

## Relationship between packing structure and porosity in fixed beds of equilateral cylindrical particles

Wenli Zhang<sup>a</sup>, Karsten E. Thompson<sup>a,\*</sup>, Allen H. Reed<sup>b</sup>, Liese Beenken<sup>a</sup>

<sup>a</sup>Cain Department of Chemical Engineering, Louisiana State University, Baton Rouge, LA 70803, USA

<sup>b</sup>Naval Research Laboratory, Stennis Space Center, MS 39529, USA

Received 16 June 2006; received in revised form 30 August 2006; accepted 10 September 2006

Available online 23 September 2006

### Abstract

Fixed beds of cylindrical particles are important in chemical engineering applications, but their packing structures are not as well understood or as well characterized as sphere packings. In this work, X-ray microtomography is used to obtain 3D images of 1.8 mm diameter equilateral cylinders in a 23 mm cylindrical container over a range of bulk porosities. A novel algorithm is used to computationally reconstruct the packings, resulting in data sets that give the location and orientation of each cylinder in the imaged packings. Extensive analysis has been performed, including bulk and local porosities, radial distribution functions, and parameters describing local and global ordering. The major factors affecting packing structure are the overall packing density and the proximity to the wall. At the highest overall packing densities, near-wall porosity becomes nearly equal to interior porosity, and significant global ordering occurs near the wall. For a vertical container, global ordering is characterized by the alignment of the particles with an orthogonal coordinate system that has one axis coincident with  $r$  (as defined by the container) and the other two axes in the  $z$ - $\theta$  plane, but rotated  $45^\circ$  with the horizontal. The observed structures are relevant in the context of flow maldistribution and heat transfer in fixed beds.

© 2006 Elsevier Ltd. All rights reserved.

**Keywords:** Packed bed; Tomography; Particulate processes; Granular materials; Packing structure; Wall effects

### 1. Introduction

The packing structure in fixed beds affects local fluid, heat, and mass transport, which in turn influences macroscopic parameters in many chemical engineering operations (e.g., separation and reaction processes). The packing structure for spherical particles is the most well studied and well understood of these systems. The minimum bulk porosity of sphere packings is 0.36 (for uniform-sized spheres), and the values for real packings typically fall into the range  $\varepsilon = 0.36$ –0.42. Packing structure near container walls exhibits partial ordering, because the locations (centers) of spheres in contact with the wall lie on a surface exactly  $\frac{1}{2}$  diameter from the wall. Typically, this partially ordered structure propagates two to four diameters into the packing.

Like spheres, cylindrical particles are prevalent in chemical engineering. In fact, they are preferable to spheres in many applications because they can be extruded. However, the packing behavior of cylindrical particles is fundamentally different from spheres because cylinders exhibit orientational freedom, and their geometry contains a variety of surface elements (i.e., flat and curved surfaces as well as corners). These differences tend to produce more diverse packing structures as evidenced by the range of porosity values reported in the literature: for equilateral cylinders, porosities range from  $\varepsilon = 0.25$  (Roblee et al., 1958) to  $\varepsilon = 0.445$  (Coelho, 1997)—a much broader range than for spheres. Diversity in packing structure is also evident from a simple visual experiment: tapping or vibrating a vial of small equilateral cylinders causes many of the cylinders that are in contact with the wall to move into either parallel or perpendicular alignment with the wall, and also to move into end–end, end–side, or side–side alignment with one another. Continued vibration results in quite dramatic global alignment patterns such as what is seen in the photograph in Fig. 1. From a practical

\* Corresponding author. Tel.: +1 225 578 3069; fax: +1 225 578 1476.  
E-mail address: karsten@lsu.edu (K.E. Thompson).

# REPORT DOCUMENTATION PAGE

Form Approved  
OMB No. 0704-0188

The public reporting burden for this collection of information is estimated to average 1 hour per response, including the time for reviewing instructions, searching existing data sources, gathering and maintaining the data needed, and completing and reviewing the collection of information. Send comments regarding this burden estimate or any other aspect of this collection of information, including suggestions for reducing the burden, to Department of Defense, Washington Headquarters Services, Directorate for Information Operations and Reports (0704-0188), 1215 Jefferson Davis Highway, Suite 1204, Arlington, VA 22202-4302. Respondents should be aware that notwithstanding any other provision of law, no person shall be subject to any penalty for failing to comply with a collection of information if it does not display a currently valid OMB control number.

PLEASE DO NOT RETURN YOUR FORM TO THE ABOVE ADDRESS.

1. REPORT DATE (DD-MM-YYYY) 10092006			2. REPORT TYPE Journal Article		3. DATES COVERED (From - To)	
4. TITLE AND SUBTITLE  Relationship between packing structure and porosity in fixed beds of equilateral cylindrical particles					5a. CONTRACT NUMBER	
					5b. GRANT NUMBER	
					5c. PROGRAM ELEMENT NUMBER	
6. AUTHOR(S)  Wenli Zhang, Karsten E. Thompson, Allen H. Reed, Liese Beenken					5d. PROJECT NUMBER	
					5e. TASK NUMBER	
					5f. WORK UNIT NUMBER	
7. PERFORMING ORGANIZATION NAME(S) AND ADDRESS(ES) Naval Research Laboratory Marine Geoacoustics Division Stennis Space Center, MS 39529					B. PERFORMING ORGANIZATION REPORT NUMBER  NRL/JA/7430-06-6	
9. SPONSORING/MONITORING AGENCY NAME(S) AND ADDRESS(ES)  Office of Naval Research 800 North Quincy Street Arlington VA 22217-5000					10. SPONSOR/MONITOR'S ACRONYM(S)  ONR	
					11. SPONSOR/MONITOR'S REPORT NUMBER(S)	
12. DISTRIBUTION/AVAILABILITY STATEMENT Approved for public release; distribution is unlimited						
13. SUPPLEMENTARY NOTES Chemical Engineering Science 61 (2006) 8060-8074						
14. ABSTRACT  Fixed beds of cylindrical particles are important in chemical engineering applications, but their packing structures are not as well understood or as well characterized as sphere packings. In this work, X-ray microtomography is used to obtain 3D images of 1.8 mm diameter equilateral cylinders in a 23 mm cylindrical container over a range of bulk porosities. A novel algorithm is used to computationally reconstruct the packings, resulting in data sets that give the location and orientation of each cylinder in the imaged packings. Extensive analysis has been performed, including bulk and local porosities, radial distribution functions, and parameters describing local and global ordering. The major factors affecting packing structure are the overall packing density and the proximity to the wall. At the highest overall packing densities, near-wall porosity becomes nearly equal to interior porosity, and significant global ordering occurs near the wall. For a vertical container, global ordering is characterized by the alignment of the particles with an orthogonal coordinate system that has one axis coincident with $r$ (as						
15. SUBJECT TERMS Packed bed; Tomography; Particulate processes; Granular materials; Packing structure; Wall effects						
16. SECURITY CLASSIFICATION OF:			17. LIMITATION OF ABSTRACT	18. NUMBER OF PAGES	19a. NAME OF RESPONSIBLE PERSON	
a. REPORT	b. ABSTRACT	c. THIS PAGE			Allen Reed	
Unclassified	Unclassified	Unclassified	UU	15	19b. TELEPHONE NUMBER (Include area code) 228-688-5473	

20090522117

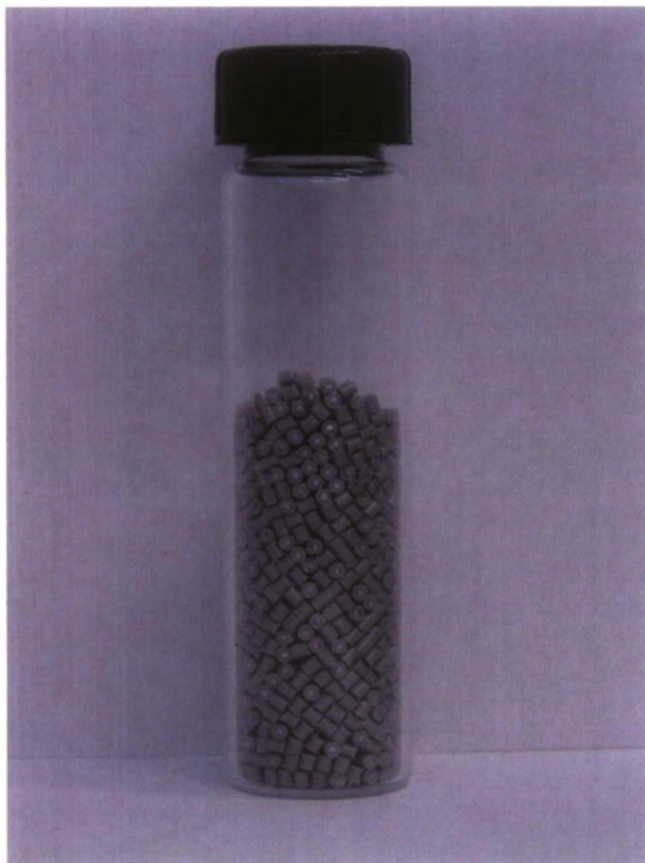


Fig. 1. Photograph of a vial of cylindrical particles, which shows the high degree of ordering that occurs at the wall as a result of vibration.

standpoint, these observations are significant because they suggest that bulk transport properties may be harder to evaluate than for sphere packings.

Despite the importance of this problem, limited quantitative analysis has been performed on density and structure variations in packings of cylinders, especially at the particle scale. The primary reason is that particle-scale data for these structures is difficult to obtain. Most particle-scale analyses performed on sphere packings have relied on numerical simulations to produce the detailed packing structure. However, the computer simulations are difficult to implement with non-spherical particles, and the Monte-Carlo methods that are currently available do not reproduce the complex, semi-ordered structures that are observed experimentally (Zhang et al., in review). Conversely, experimental studies are able to create the complex packing structures of interest; however, recovering particle-scale data using traditional methods is difficult and time consuming.

In this work, we address this problem using a two-step process. First, X-ray microtomography imaging is performed on a series of packed beds of equilateral cylindrical particles. This approach allows real (rather than computer-simulated) packings to be used. At the same time, it provides the necessary

resolution to obtain particle-scale data. Second, a novel computational method is used to reconstruct the packings from the microtomography images on a particle-by-particle basis. The resulting data sets contain the location and orientation of each cylinder in a packing, which is sufficient to completely characterize both the packing and void structure of the bed.

Using these data sets, we have analyzed changes in the packing structure as a function of increasing packing density. The cylindrical particles have dimensions  $L \approx D \approx 1.8$  mm. The container is 23 mm in diameter. Hence, wall effects are significant, and much of the current analysis is aimed at this issue.

## 2. Background

### 2.1. Packings of spheres

Sphere packings are the most-studied type of particle packing. Ordered structures include rhombohedral packings and cubic packings, which bracket the range of attainable porosities at  $\varepsilon_{\min} = 0.2595$  and  $\varepsilon_{\max} = 0.4764$ , respectively. Disordered packings exhibit a much smaller porosity range with most packings of interest falling into the range  $\varepsilon = 0.36$ – $0.40$ . The terminology random close packed (RCP) is widely used to denote the highest packing density (lowest porosity) that can be achieved with spheres in the absence of global ordering. No theory has provided an exact value, but the well-accepted limit is  $\varepsilon_{\text{RCP}} = 0.36$ , plus or minus some small amount that varies according to the source consulted.

The terminology *random* has been used rather loosely in sphere-packing studies, the implication being that packing structure remains random even as the porosity decreases over the commonly observed range. Although sphere packings are probably less susceptible to local or global ordering than are cylinder packings, there is evidence of structure as the packing density increases. Clarke and Jonsson (1993) observed a steady increase in the number of icosahedral clusters and icosahedral fragments in computer-generated sphere packings as the packing density increased. Torquato et al. (2000) studied jammed packings over a range of packing densities, and reported a steady increase in the parameter  $Q_6/Q_6^{\text{fcc}}$ , which quantifies the local bond-orientational order as compared to a perfect fcc crystal. Liu and Thompson (2000) used small periodic sphere packings (216 spheres) to achieve porosities as low as  $\varepsilon = 0.3508$  (nearly 1% below the traditional RCP limit) and observed an onset of global ordering in these structures, even without the formation of a distinct lattice structure.

Torquato et al. (2000) addressed the ambiguity in the terminology *random packing* by proposing that the maximally random jammed (MRJ) state be used as a more rigorous definition to characterize dense, disordered structures. An MRJ value would be found by minimizing some measure of order over an ensemble of physically jammed states. For spheres, they obtained a value  $\varepsilon_{\text{MRJ}} = 0.36$ , which is in agreement with the general definition of  $\varepsilon_{\text{RCP}}$ , but is slightly greater than the

lowest RCP values that have been found by simulation and experiment.

Spheres near a containing wall form more ordered structures than spheres in the internal region of random packings. From a simplistic point of view, this effect is caused by a significant fraction of particles necessarily contacting the container walls, which leads to alignment on a plane or cylindrical surface, depending on the wall geometry. A second layer of spheres will tend to lodge themselves in the deepest pockets formed by the wall spheres, creating a less organized but distinct structure, and so on. These wall effects tend to die out a few sphere diameters into the packing, depending on the bulk packing density. This effect can be quantified with a wall radial distribution function (RDF) or density function. The wall RDF quantifies the probability of finding a sphere center at a given distance from the wall. It contains at least two or three distinct peaks corresponding to the layers described above. Numerous experimental studies have examined RDFs in cylindrical containers (e.g., Roblee et al., 1958). Kubie (1988) derived a theoretical wall density function and compared it to experimental results. Reyes and Iglesia (1991) and Mueller (2005) computed wall density functions for numerically generated loose, random, sphere packings within cylindrical containers. Zou and Yu (1995) discuss the effects on packing structure that are caused by the base of a cylindrical container.

The impact that these wall effects have on the overall porosity depends on the ratio of the tube diameter ( $D_t$ ) to particle diameter ( $D_p$ ). Dixon (1988) developed semi-empirical equations to quantify this effect for spheres, cylinders, and hollow cylinders. For spheres, a maximum overall porosity of  $\varepsilon \approx 0.67$  occurs at  $D_t/D_p \approx 1.72$ . Theuerkauf et al. (2006) used the discrete element method (which accounts for particle–particle and particle-wall mechanical interactions) to quantify particle-scale structure and porosity in a series of beds with  $D_t/D_p$  in the range three to 20.

## 2.2. Packings of ellipsoids and spherocylinders

Non-spherical particles exhibit rotational degrees of freedom as well as translational freedom, which affects their packing structure. It has long been known that random packings of long slender particles (for instance,  $L/D > 10$ ) exhibit much lower packing fractions than spheres or other compact particles (Milewski, 1973). A number of theories have been developed to explain this behavior, including those presented by Evans and Gibson (1986) and Philipse (1996).

More recent work has shown that when ellipsoids or spherocylinders are only slightly elongated ( $1.0 < L/D < \sim 2.5$ , depending on the particle shape), the packing density increases (Williams and Philipse, 2003; Donev et al., 2004). In these situations, the porosity can reach values as low as  $\varepsilon = 0.27$  (Donev et al., 2004, for ellipsoids). The consensus explanation for this behavior is the additional rotational degrees of freedom that exist for non-spherical particles. Williams and Philipse (2003) make an analogy to polydisperse sphere packings, noting that either size variation or orientational freedom allows particles to be packed in more tightly than

with monodisperse spheres. Donev et al. (2004) note that the additional degrees of freedom require more contacts per particle to achieve a jammed state (or equivalently, a static equilibrium, Weitz, 2004), which by inference requires a denser packing.

## 2.3. Packings of cylinders

Packings of rigid cylinders have been the subject of a number of experimental studies. Roblee et al. (1958) impregnated packed beds with wax, and then extracted annular sections of the beds to generate radial density functions. A range of particle shapes found in chemical-engineering applications were used. For equilateral cylinders, their results indicate that edge effects penetrate three particle diameters from the wall. They also report a mean porosity of  $\varepsilon \approx 0.25 \pm 0.025$  (95% C.I.) in the interior of the packing. Kondelik et al. (1968) suggested that particles will align orthogonal to the wall, and used this assumption to predict the location and value of minima in local porosity distributions. Stephenson and Stewart (1986) used packings of cylinders in flow experiments. The experimentally measured porosities in their beds ranged from  $\varepsilon = 0.348$  to  $\varepsilon = 0.361$ . Dixon (1988) performed packing experiments and developed a correlation for porosity as a function of container-to-particle diameter ratio. His results indicate a porosity of 0.36 for large containers. (No attempt was made to vibrate the cylinders into a dense packing in the experiments.) Foumeny and Roshani (1991) present similar correlations for equilateral as well as longer and shorter cylinders. They report a maximum interior porosity of 0.293 in the limit of large beds, when the ratio of the tube to particle diameter was large ( $\sim 30$ ). Voidage was determined by infiltrating a packed bed with a known quantity of water. Benyahia (1996) impregnated packings of lead cylinders with resin, sliced the packings at 1 mm intervals along the axial direction, and used two-dimensional image-analysis software to study the packing structure from planar images. Their focus was on non-equilateral particles, but results from spheres and equilateral cylinders are given for comparison. For equilateral cylinders, they report porosity values from Roshani (1990) in the range 0.278 to 0.422, which were obtained from a water-weight loss technique (i.e., porosity was determined from water weight loss after the water-saturated sample was dried). They provide wall radial density functions for a number of the packings. Nijemeisland et al. (2004) studied a series of packed beds of cylinders with ( $D_t/D_p = 4$ ), and then used the most commonly observed packing structure in CFD simulations of stream reforming.

Fewer studies have examined changes in porosity due to vibration or other densification processes. Nardin et al. (1985) studied loose and dense packings for a series of fibers and cylinders. For polypropylene cylinders with  $L/D_p = 1$ , they report maximum and minimum porosities of 0.462 and 0.371, respectively. Villarruel et al. (2000) studied packings of moderate-aspect-ratio cylindrical particles ( $L/D_p = 3.89$ ), which were packed in a vertical cylindrical container ( $D_t/L = 2.71$ ). Experiments were performed by vibrating loose packings ( $\varepsilon \sim 0.5$ ) into highly ordered, high-density configurations (porosity

reduced to nearly 0.25). They showed that during the vibration, ordering begins at the wall with the cylinders aligning vertically. For low accelerations this nematic alignment process occurs throughout the entire packing. However, at higher accelerations the interior of packing does not reach a fully ordered state. **Montillet and Le Coq (2001)** performed non-destructive imaging of a packed bed of cylinders with aspect ratio  $L/D = 5.29$ . They analyzed individual slices (perpendicular to the column axis), which showed significant variations in the radial porosity distribution from one section to another in the bed. This effect has implications on solute dispersion during flow through a bed. **Sharma et al. (2001)** performed water-substitution and MRI experiments on packings of equilateral cylinders. They varied container diameter and also induced density changes by tapping. Changing column diameter produced porosities ranging between 0.28 and 0.33. Tapping the columns generally reduced porosity by 2–4%. **Lumay and Vandelwalle (2004)** studied the packing of cylinders with  $L/D_p > 1$ , including cases when the container diameter was smaller than the cylinder length. Maximum packing densities were observed in cases in which the cylinder length was approximately equal to the container diameter. When this parameter was fixed ( $L/D_{\text{container}} = 1$ ), the porosity increased for higher-aspect ratio particles (the same effect observed in the absence of wall effects).

Relatively few computational and theoretical studies exist for rigid cylinders, partly because their geometry is less amenable to the required computations as compared to sphereocylinders and ellipsoids. **Coelho et al. (1997)** generated packings of equilateral cylinders with  $\varepsilon = 0.445$  using a sequential deposition (SD) technique. SD algorithms are known to produce high porosity packings. Hence, their data ( $\varepsilon = 0.445$ ) may provide a good upper bound for attainable porosity. **Blaak et al. (1999)** performed molecular dynamics simulations with rigid cylinders of aspect ratio  $L/D_p = 0.9$ . They report a range of interesting structures, but the packings densities are not representative of macroscopic particulate packings. In our own collective rearrangement simulations, we have obtained a minimum porosity of  $\varepsilon = 0.35$  for random packings of equilateral cylinders (a cubic domain with periodic boundaries). A slight (but statistically relevant) decrease to  $\varepsilon = 0.34$  is obtained by increasing the particle aspect ratio to  $L/D_p = 1.2$ .

#### 2.4. Non-destructive imaging

X-ray computer tomography and 3D magnetic resonance imaging techniques have proved invaluable for analyzing packed beds (**Montillet and Le Coq, 2001; Sharma et al., 2001; Wang et al., 2001**), particulate materials (**Thompson et al., 2006**) and/or fluid distributions (**Marchot et al., 1999**). For spherical particles, simple algorithms can be used to extract the location of each sphere in a packing, thus providing a relatively automated technique for obtaining particle-scale information about large, physically realistic packings (**Seidler et al., 2000; Richard et al., 2003; Aste et al., 2004**). However, we have shown that these simple reconstruction techniques do not allow particle-by-particle identification of cylindrical particles (**Thompson et al., 2006**). For this reason, we use cylinders

with an aluminum core, which allows for accurate computation of position and orientation of each particle, as described next.

### 3. Experimental method

#### 3.1. Cylinders

The cylindrical particles were constructed with an outer layer of PEEK polymer and an inner aluminum core. This choice of materials was made so that the core could be identified separately from the physical cylinder in the microtomography images, which serves two purposes. First, it makes the task of computationally separating one particle from another easier by reducing the volume fraction of the foreground phase (which is especially relevant for the high-density packings in which particles are stacked in alignment with one another). Second, identification of the thinner core allows more accurate computation of the cylinder orientation using the techniques described below. (It should be noted that a separate algorithm has been developed for computer reconstruction of individual particles, **Thompson et al., 2006**, which could be used with uniform-density cylinders if necessary.)

The cylinders were made using PEEK tubing (Upchurch Scientific) with 1.8 mm OD and 0.76 mm ID. A 0.635 mm OD aluminum welding rod was coated with craft adhesive and fed into the tubing. The tubing was then cut into 1.8 mm long cylinders using an electric tubing cutter. A groove was mounted onto the tubing cutter along with a stop/release lever that allowed the tubing to be fed to the proper position before cutting. This arrangement made the cutting process reasonably automated and accurate. The dimensions of 40 of the cut cylinders were measured, giving the following results:  $D = 1.77 \text{ mm} \pm 0.0021 \text{ mm}$ ;  $L = 1.80 \text{ mm} \pm 0.0024 \text{ mm}$  (where the  $\pm$  range is the standard deviation in the measurement).

#### 3.2. Packing experiments

An acrylic cylindrical container with a solid bottom and open top was machined to dimensions of 23 mm ID and 60 mm depth. The PEEK/Al cylinders (see Fig. 1) were packed into the container in a range of porosities, using the following techniques.

For the loosest packings, two methods were tested. In one case, the cylinders were allowed to settle into their packing structure in degassed, deionized water, which reduced the net gravitational forces (as compared to packing the particles in air). This settling was performed with the container already placed on the tomography stage, which prevented subsequent vibrations from rearranging the packing. This technique was used to produce the loosest of the packing structures (C1) discussed below. The other technique that was tested was to place a vertical rod in the center of the container and to gently pour the cylinders in the annular space around the rod. The rod was then slowly removed from the packing (as it sat on the tomography stage), allowing cylinders to rearrange and fill in the space that had been occupied by the rod. A packing generated in this

way was imaged and characterized. The resulting packing had two distinct regions with different porosities and structures. The original annular space exhibited a porosity  $\varepsilon = 0.416$  as well as significant ordering. The space where the rod had been exhibited the highest internal porosity of any sample,  $\varepsilon = 0.385$ , but also contained uncharacteristically large voids. While interesting, we believe that these results are related to the specific packing technique and are not typical of most fixed-bed structures. Therefore, these data are not included in the subsequent analysis.

Four other packings were created by gently pouring cylinders into the container (in air) and then allowing vibration-induced settling in some cases. The C2 sample was poured gently into the container without subsequent vibration. The C3–C5 samples were exposed to varying degrees of tapping and/or vibration. No attempt was made to quantify the amount or rate of energy that was applied to the system. The heights of the packings were measured simply to obtain a priori estimates of the packing densities (i.e., before imaging and image processing). It is worth noting a qualitative observation: a high-energy vibration (a Vortex Genie 2 test-tube mixer) did not provide for the highest density packings. Instead, our highest-density packing (C5) was obtained by mounting the container firmly in the tomography chuck and then tapping it repeatedly with a rigid tool such as a metal rod. This behavior is intuitively reasonable and is also consistent with the results from Villarruel et al. (2000), who quantified the accelerations that their packings were exposed to.

### 3.3. Microtomography

The XRT system used in these experiments is comprised of an X-ray tube (i.e., FeinFocus 10–225 keV, 0–3 mA with 3  $\mu$ m X-ray aperture), a 23-cm diameter Image Intensifier, a sample stage that provides 6-fold axis of movement and a computer that collects and converts X-ray attenuation data into images. The X-ray production occurs in a lead-shielded room, while the conversion of attenuation data into images occurs outside the lead-shielded room, in the control room. Also, within the control room, a video projection of a two-dimensional X-ray image is displayed onto a monitor for real-time assessment of the sample.

Maximum sample resolution is obtained by placing the sample in close proximity to the X-ray aperture such that the X-ray projection, a cone beam, narrowly spans the sample width. After the sample is scanned at one elevation, successive vertical translations and scanning of the sample are made until the desired sample length is obtained. The sample attenuation data is then converted to two-dimensional images, which are later combined into a single volumetric image.

Scans were performed on three separate occasions. The data sets used here were selected from different scan dates and therefore have differing voxel resolutions. The C1 data have a resolution of 0.0454 mm (i.e., each voxel in the image is a  $9.36 \times 10^{-5} \text{ mm}^3$  cube). The C2–C4 data have a voxel resolution of 0.0466. The C5 data have a resolution of 0.0406 mm.

## 4. Computational methods

### 4.1. Tomography data

Computed tomography data, while volumetric in nature, begins as a series of two-dimensional images or slices (Fig. 2a), which are extremely well registered and can be easily joined into a volumetric image simply by knowing the spatial distribution of these slices in the vertical direction. While computed tomography data collected for this experiment are subject to “beam hardening” or the effects of differential X-ray attenuation that occurs to some degree in all polychromatic energy systems (Wellington and Vinegar, 1987), this artifact can be minimized during initial calibration and virtually eliminated by post-process image analysis. Because the aluminum cores show up brightly (they have a higher attenuation than the other material in the system), they can be easily segmented or isolated from the PEEK tubing that surrounds them. In this process, the three-dimensional grayscale image is converted to a 1-bit binary image by choosing a threshold X-ray absorbance between the values for PEEK and aluminum. In the resulting binary images, the voxels in the aluminum cores are assigned to the foreground phase while both the PEEK voxels and the void-space voxels are assigned to the background. Fig. 2b depicts the three-dimensional binary view of the aluminum cores from a small section of one of the packings.

Each core in the Fig. 2b image is composed of a series of cubic voxels. The size of each aluminum core is 1.8 mm length  $\times$  0.635 mm diameter, giving a volume of  $0.5700 \text{ mm}^3$ . Using the known voxel resolution, the number of voxels per core can be computed. For instance, for packing C5, a voxel resolution of 0.0406 mm means that the typical size of an aluminum core should be 8517 voxels. (For a different resolution, the expected number of voxels per aluminum core would be different.) This information is used during the computational reconstruction of the cylinders, as described below.

### 4.2. Computational reconstruction of the packing

The computer reconstruction process begins with a foreground-phase (aluminum) “burn” of the binary volume data (i.e., the data shown in Fig. 2b) (Lindquist and Lee, 1996). This procedure is equivalent to computing a non-Euclidian distance map for the foreground phase in which each Al-phase voxel is labeled with a measure of the distance to the nearest foreground-background interface (i.e., surface of an aluminum core).

The identification of individual aluminum cores proceeds as follows. A connected-components algorithm is run to identify islands of foreground voxels. If every aluminum core in the image were separated from its neighbors by at least one background-phase voxel, then the connected components algorithm alone would be sufficient to assemble the individual cores. However, this is not the case, as shown by a histogram of the number of connected components versus the number of voxels per connected component (Fig. 3). A dominant peak is

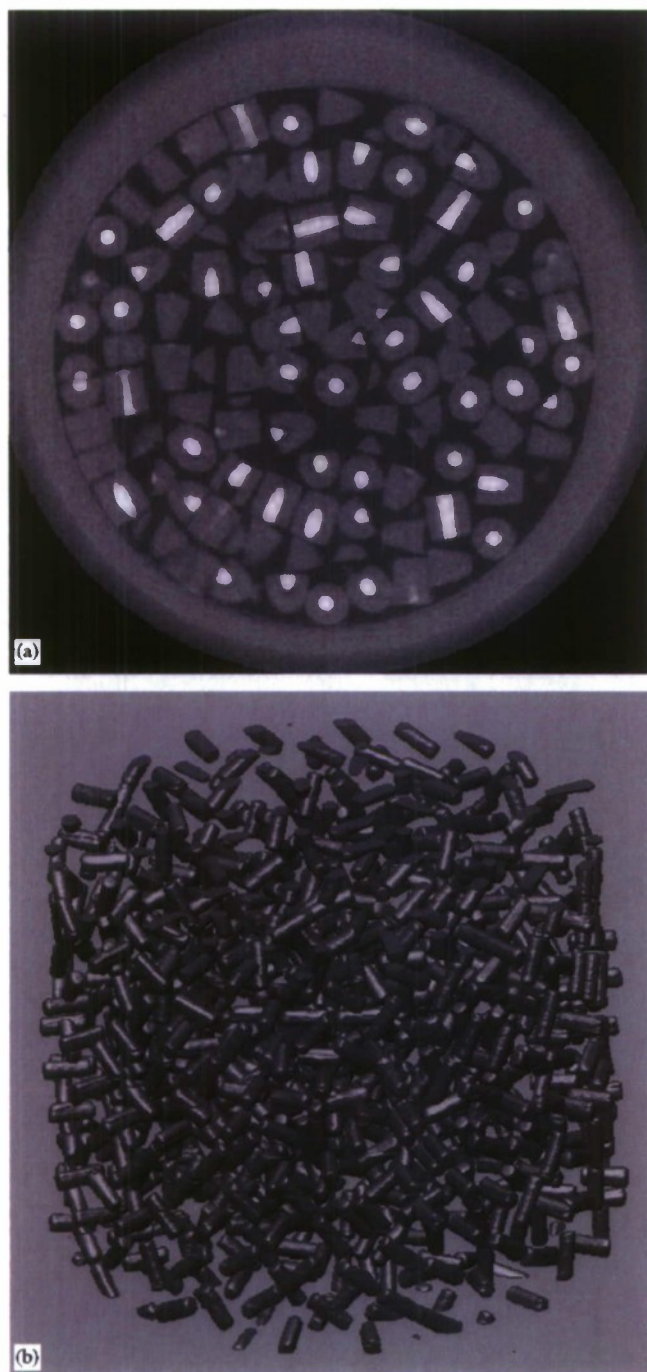


Fig. 2. (a) Gray-scale image of a single slice from one of the tomography images. The aluminum cores show up brightest (white). The PEEK tubing (and the acrylic container) show up as the lighter shade of gray. The air in the void space shows up as darker gray; (b) three-dimensional view of aluminum cores from a section of packing C5.

present near the estimated value of 8517 voxels per aluminum core. Smaller secondary peaks are also observed near 20,000, 31,000, and 44,000 voxels, which represent 2-, 3-, and 4-core clusters that are not separated by the connected-components algorithm. (The numerical values suggest that the number of vox-

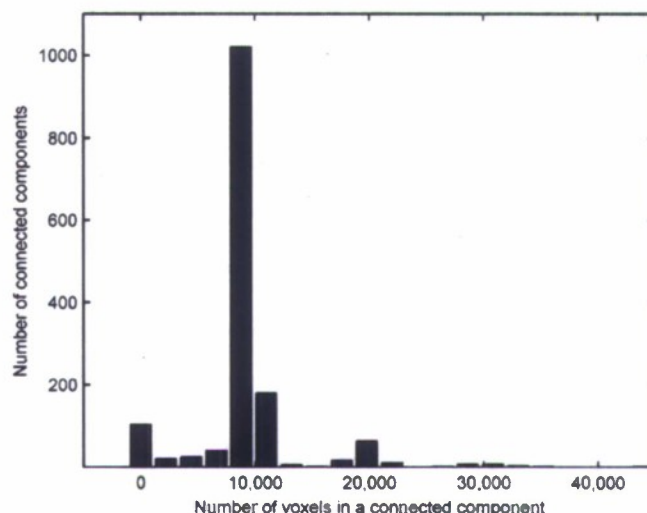


Fig. 3. Histogram of number of connected components versus size of connected components (in number of voxels) for the C5 image.

els per aluminum core is around 10,000 rather than 8517. This discrepancy likely stems from a combination of factors: imprecision in the diameter of the aluminum welding wire; slight variations in the cut length of the cylinders, and the thresholding process used to make voxel assignments from the original grayscale image.) The small connected components to the left of the main peak are incomplete aluminum cores that were cut by the top and bottom of the image—these are automatically discarded during the reconstruction process by cropping out connected components whose centers are near the top and bottom of the data set.

The problem of the large connected components is addressed by defining a range of allowable sizes  $\Delta N_{cc}$ , which brackets the estimated size for connected components, spanning a reasonable range so as to account for the distribution of sizes that will be found in an experimental data set. For the Fig. 3 histogram, this range might be defined as 7000–12,000 voxels. Additionally,  $\Delta z_{crop}$  is specified, which defines regions at the top and bottom edges of the data set where partial cores (i.e., those on the far left of the Fig. 3 histogram) are likely to be found because they are cut by the edge of the image. For the results shown below,  $\Delta z_{crop}$  was set to one cylinder diameter.

To assemble the complete set of individual aluminum cores, the following procedure is adopted.

1. Connected components are assembled using the foreground voxels, and any connected component that falls into the allowed size range defined by  $\Delta N_{cc}$  and which is not discarded by the  $\Delta z_{crop}$  criterion is accepted as an individual aluminum core.
2. All foreground data that were not assigned during step 1 are eroded one level. A connected-components analysis is then run on the eroded data, after which components are dilated to add back the eroded voxels. Any dilated clusters that satisfy the  $\Delta N_{cc}$  and  $\Delta z_{crop}$  criteria are accepted as additional individual aluminum cores and tagged as such.

This procedure is repeated for increasingly deep erosions (a level-two erosion, level-three erosion, etc.).

3. Step two ends when the erosion level is so deep that it removes all unassigned foreground voxels from the image. (In our experiments, it is typical to have a few remaining large clusters that exceed the  $\Delta N_{cc}$  criterion but that were not broken up, even by the deepest erosion possible. These are split by an automated process, but are then checked by hand to ensure they represent single aluminum cores.)
4. A table of all unclaimed foreground connected components is printed to help validate the computational reconstruction process. For successful reconstructions, these unclaimed clusters should be one of two types: larger clusters that were eliminated by the cropping criterion  $\Delta z_{crop}$  or very small clusters (less than 10 voxels) that are attributable to noise in the image. All five reconstructions shown below were successful according to this definition.

Following identification of aluminum cores, the position of each cylinder is recorded as the center of mass of its respective voxel cluster. The orientation of each cylinder is found by performing an optimization that minimizes the sum of the squares of the distance from the vector along the cylinder axis (unknown) to each voxel in the cluster. The cylinder diameters are assigned based on the known diameter of the PEEK tubing. The final data set consists of seven scalar parameters per particle in the packing: three components for the position vector of the cylinder, three components for its axis-orientation vector, and its radius.

All subsequent computations and visualizations are performed using the particle-scale data (as opposed to the voxel data). Certain statistical computations described below are performed in cylindrical coordinates. Hence, the  $x$ – $y$  location of the container axis must be known. It is found by minimizing the circle that contains all particle centers when projected onto the  $r\theta$  plane.

## 5. Statistical analysis

The five packings described here are denoted C1–C5 in order of decreasing porosity (increasing packing density). Fig. 4 contains images of packings C1, C3 and C5. As with the quantitative data, these images were created directly from the particle-scale data (particle positions and orientations) rather than from the tomography images themselves. The top views of the packings in Fig. 4 are an excellent illustration of the onset of ordering that occurs as packing density is increased.

For each of the five packings, a range of parameters were computed to help interpret and quantify the changes in packing structure as a function of packing density. Many of these are plotted as a function of  $\xi \equiv (R - r)/D_p$ , which is the non-dimensional distance from the wall (or, likewise, distance from the wall in units of cylinder diameter). Some of the parameters are meant to probe for local structure (i.e., how particle location and/or orientation is influenced by its neighboring particles). Other parameters are meant to probe for global structure (i.e., particle location and/or orientation with respect to global co-

ordinates or boundaries, including the container walls). These parameters are described briefly in this section.

### 5.1. Porosity

Porosities of each packing are reported as bulk and incremental values. The bulk values are averaged over annular volumes with  $\Delta r \geq 2D_p$ . Local (incremental) values are averaged over annular volumes in which  $\Delta r$  is significantly smaller than the particle diameter.

### 5.2. Radial distribution function

The RDF defines the number density of particle centers versus position. Two RDF functions are used: the wall RDF and the particle RDF. To compute the wall RDF, the container is divided into a series of concentric annuli of equal thickness  $\Delta\xi$ . The particle centers in each ring are counted and the normalized RDF is computed as

$$g(\xi) = \frac{N(\xi)}{\rho \cdot V_{ring}(\xi)}, \quad (1)$$

where  $N$  is the number of particles in the ring  $V_{ring}$  and  $\rho$  is the mean number density.

The particle RDF is a similar parameter, but it quantifies the number density of particle centers with respect to distance outward from a single particle. The particle RDF is straightforward to compute and interpret for uniform-sized spherical particles: a peak at 1 particle diameter is indicative of the layer of spheres in direct contact with the test sphere (whose centers are necessarily one diameter from the center of the test sphere). It is less straightforward to calculate and interpret for cylindrical particles because two particles in contact can have a range of center-to-center distances depending on the contact geometry. Thus, to compute the particle RDF for cylinders, we interpret pair separation as the minimal distance from the surface of the test particle to the center of another particle (a definition that aids in normalizing the RDF using the excluded volume, Williams and Philipse, 2003).

### 5.3. Local orientational ordering

Local ordering is measured by comparing (for each test cylinder in a region of interest) the relative orientation of cylinders that lie in its proximity. Local axial alignment is quantified using a nematic ordering parameter  $S_2$ :

$$S_2 = \frac{1}{2} \langle 3 \cos^2 \theta_{ij} - 1 \rangle = \frac{3}{4} \langle \cos 2\theta_{ij} + \frac{1}{3} \rangle. \quad (2)$$

The angular brackets signify averages over a local neighborhood. There exists no precise definition of a local neighborhood. In results presented below, particle-separation distance will be used as a mechanism for identifying neighboring particles, and two different criteria will be used for comparison: gap width  $\leq 0.05D_p$  and gap width  $\leq 0.5D_p$ .

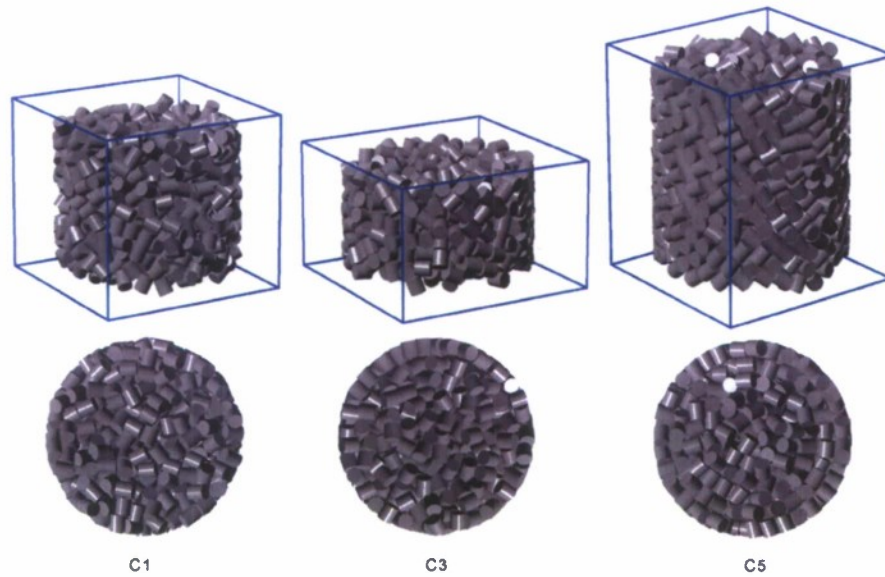


Fig. 4. Images of packings C1, C3, and C5 generated from the particle-scale data sets obtained after reconstruction. The top views show the top of the particle-scale data. Physically, however, this view corresponds to an elevation in the interior of the packing because the tomography process imaged an interior section of the experimental packings and also because tomography data were cropped in the  $z$  direction during the computer reconstruction process.

We use the terminology *orthogonal ordering* to denote alignment in which particle axes are either parallel to one another or perpendicular to one another (thus forming a locally or globally orthogonal coordinate system). Local orthogonal ordering between neighboring cylinders is defined by  $S_4$ :

$$S_4 = \frac{1}{8} \langle 35 \cos^4 \theta_{ij} - 30 \cos^2 \theta_{ij} + 3 \rangle. \quad (3)$$

In both formulas,  $\cos(\theta_{ij})$  is the inner product of the normal vectors for the axes of the neighboring cylinders.

#### 5.4. Global orientational ordering

Global ordering refers to the presence of systematic structure at the bed scale, which may include positional ordering (e.g., a partial or complete lattice structure) or orientational ordering such as a nematic (aligned) phase.

Global orientational ordering can be quantified using modified spherical harmonics (see, for instance, Blaak et al., 1999). Specifically, the parameters  $I_2$  and  $I_4$  are used to probe the packing for global ordering in a frame-independent Cartesian system. These are defined as

$$Y_l^m(\theta, \phi) = \sqrt{\frac{2l+1}{4\pi} \frac{(l-m)!}{(l+m)!}} P_l^m(\cos \theta) e^{im\phi},$$

$$I_l = \left[ \frac{4\pi}{2l+1} \sum_{m=-l}^l |Y_l^m(\theta, \phi)|^2 \right]^{1/2}, \quad (4)$$

where  $\theta$  and  $\phi$  are the zenith and azimuth, respectively, of a cylinder's axis and  $P_l^m$  are the associated Legendre

polynomials. From a physical perspective, finite values of  $I_2$  are indicative of global nematic ordering and finite values of  $I_4$  are indicative of orthogonal ordering with respect to a global coordinate system.

The disadvantage to using  $I_2$  and  $I_4$  for the present data is that we expect the primary source of any global ordering in the system to originate at the container wall, and therefore to be aligned with the cylindrical coordinates defined by the container. Consequently, we define three additional sets of parameters. The first set probes for alignment with or orthogonal to the container axis. Specifically,  $S_{2,z}$  and  $S_{4,z}$ , are defined in the same way as  $S_2$  and  $S_4$  above except that the angles are replaced by  $\theta_{iz}$ , which is the angle between a particle axis and the container axis.  $S_{2,z}$  probes for a dominant vertical orientation of the cylinders (i.e., alignment with the container axis).  $S_{4,z}$  probes for a combination of vertical cylinder orientation and orientation orthogonal to the vertical direction (i.e., cylinders lying in the horizontal plane). The second set probes for ordering that is triggered by wall.  $S_{2,r}$  probes for a dominant radial alignment;  $S_{4,r}$  probes for a combination of radial alignment (denoted  $r_{||}$  alignment) along with alignment orthogonal to  $r$  (denoted  $r_{\perp}$ ). As with the first set, these two parameters are defined using the  $S_2$  and  $S_4$  definitions but with the angles replaced with  $\theta_{ir}$ . Both  $S_{2,r}$  and  $S_{4,r}$  can be computed as functions of  $r$ , which is a useful property for assessing how far wall effects propagate into the bulk packing.

Finally, we define  $S_{4,\alpha}$ , where  $\alpha$  is the angle between an arbitrary alignment direction and a reference plane or axis. For instance, we will use  $S_{4,\alpha}$  below to test whether particles orthogonal to  $r$  have a preferred orientation relative to  $z$ . As before, the function is defined using Eqs. (2) and (3) but with the  $\cos(\theta_{ij})$  values replaced by  $\cos(\theta_{i\alpha})$ .

## 6. Discussion

### 6.1. Bulk porosity

Bulk porosity is an important parameter in chemical-engineering applications. Permeability is a strong function of porosity as shown by scaling in the Carman–Kozeny or Ergun equations. Additionally, porosity variations are a major factor that contributes to flow maldistribution in packed beds and columns. Using the current data, we examine the range of bulk porosities that were attained with equilateral cylinders as well as how the range differs depending on proximity to the wall.

The overall porosity range for the five packings is 0.285–0.406, which is significantly broader than the range observed for sphere packings, but not as broad as the range that can be found in literature as reported above. A further breakdown of the porosity values is obtained by computing a near-wall porosity in the annular region  $0 < \xi < 2$  as well as an internal region inside this annulus. Table 1 contains the numerical porosity values for the annular and internal porosities in the bed. The values emphasize an important point regarding porosity variation in a single packed bed: a general rule of thumb is that near-wall porosity is higher than interior porosity (one of factors leading to flow maldistribution in packed beds). However, because the wall porosity varies over a wider range than the interior porosity, the two highest-density packings exhibit nearly uniform porosity over the cross section of the bed. This result suggests that vibrating a packing of cylinders into a higher-density state is one way to help eliminate porosity variations in a fixed bed of equilateral cylinders. It is important to note, however, that despite the uniform porosity, the packing structure in the near wall region is significantly different than in the interior for these high-density packings (as shown later). Hence, without more involved experiments or simulations, it is difficult to assess how this structure affects heat transfer or fluid-flow distributions.

### 6.2. Radial porosity distribution

Fig. 5 contains plots of local porosity versus  $\xi$  for the five different packings. All five plots show oscillations in porosity near the wall, which is expected because of the near-wall layering. For the highest density packings, the porosity fluctuations extend at least five layers into the packing. For the minimum density packings, they extend somewhere between 2 to 4 particle diameters into the packing. A more subtle but significant difference is the shape and magnitude of the porosity profile at the wall for the different packing densities. The high-density packings have a maximum porosity  $\varepsilon \approx 0.8$  at the wall and the profile decreases steeply to a minimum value slightly greater than 0.1, which occurs near  $\xi = \frac{1}{2}$ . In contrast, the maximum near-wall porosities in the loose packings exceed 0.9 (it exceeds 0.95 for the C1 packing), and the profiles are not as steep: the minimum porosities remain larger than 0.25 and occur at approximately  $\xi = \frac{3}{4}$ . The differences can be attributed to the more disordered structure in the high-porosity packings: cylin-

Table 1

Bulk porosities broken down into three values for each packing: overall porosity, near-wall porosity, and interior porosity

Packing	Porosity		
	Near wall ( $\xi \leq 2$ )	Internal ( $\xi > 2$ )	overall
C1	0.441	0.364	0.406
C2	0.394	0.340	0.369
C3	0.368	0.315	0.343
C4	0.300	0.307	0.304
C5	0.289	0.279	0.285

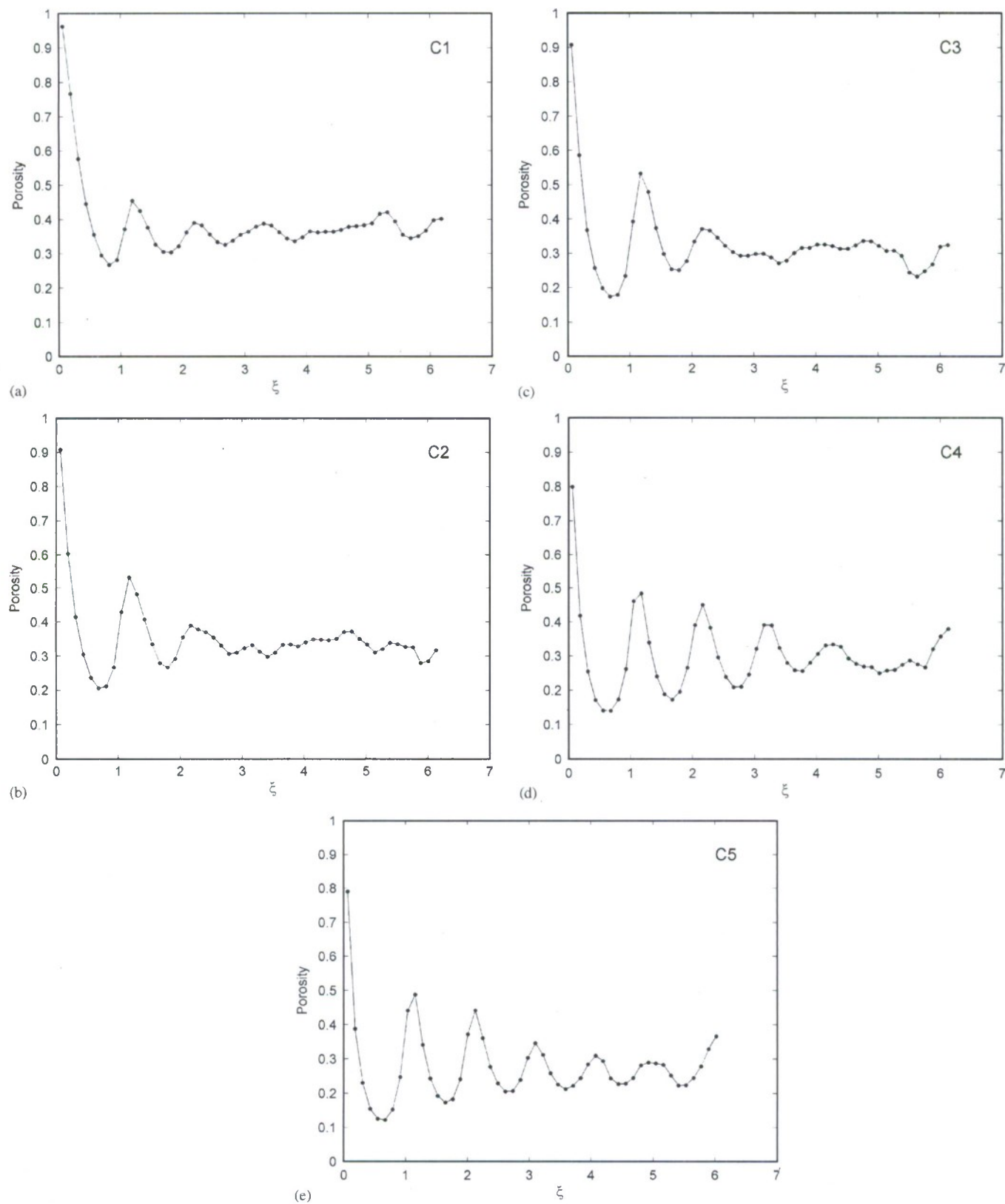
ders that contact the wall, but are neither parallel nor orthogonal to the wall, make contact at a single corner point on the cylinder. This geometry leads to a higher wall porosity, a broader, shallower minimum porosity, and pushes the minimum farther from the wall.

### 6.3. Positional ordering—global

The characteristic shape of the radial porosity distributions in Fig. 5 is attributable to alignment of the outer ring of particles against the container wall and propagation of this ring-like structure at least a few particles inward. At higher packing densities, this ring-like structure becomes more prevalent and is observed at greater distances away from the container wall. A powerful way to qualitatively express this effect is to plot the position of every particle on the  $r$ – $\theta$  plane, as shown in Fig. 6 for the C1 and C5 packings. In the maximum-density packing, the outer two rings are nearly perfect, and ring structure remains evident four particle diameters away from the wall. In contrast, only the outer ring (particles in direct contact with the wall) is apparent in the C1 packing.

A quantitative expression of this same effect is the RDF. Plots of the wall RDF are shown in Fig. 7. Qualitatively, the same effects seen in Figs. 6 and 7 are present. Quantitatively, the RDF plots show nearly double the probability of finding a particle center at  $\xi = \frac{1}{2}$  for the C5 packing as compared to C1. Because both packings necessarily have a reasonably large number of particles in contact with the wall, this difference points to the alignment of the particle axes either parallel or perpendicular to the wall, either of which will place the particle center at  $\xi \approx \frac{1}{2}$ ; other orientations will move the particle center to larger values of  $\xi$ .

An important difference between cylinder and sphere packings can be seen in Figs. 6 and 7. For a sphere packing, the second peak in the wall RDF has a distinct shoulder. The primary maximum on this peak corresponds to spheres nestled into a well formed by three-spheres in contact with the wall, and will be located near  $\xi = 1.3165$ . The shoulder corresponds to a fraction of spheres that are not able to pack as closely to the wall and therefore push the shoulder of the peak toward  $\xi = 1.5$ . For cylinders, a strong peak at  $\xi \approx 0.5$  means that this first layer of spheres are packed with their sides or ends aligned with the wall. (The exact location of the peak will depend on the curvature of the container wall as well as the orientation of the particles—see the later

Fig. 5. Porosity distributions ( $\epsilon$  versus  $\zeta$ ) for the five packings.

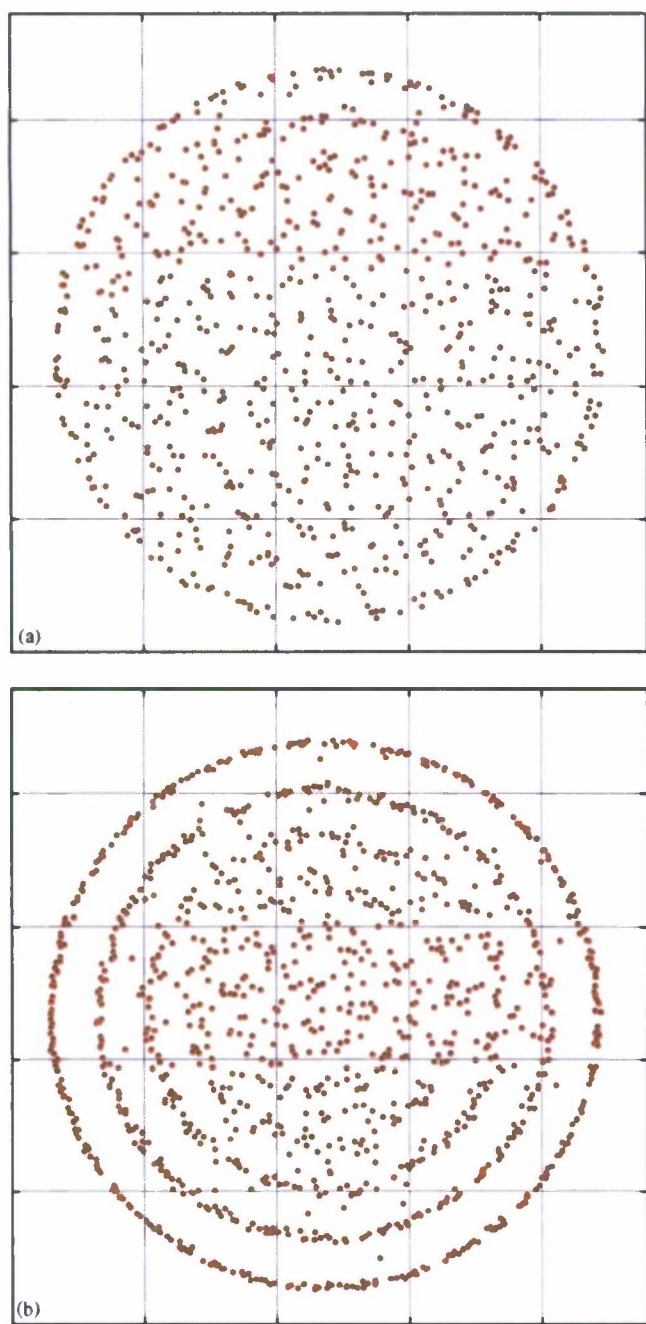


Fig. 6. Distribution of particle centers projected onto the  $r\theta$  plane for the minimum-density (C1, top) and maximum-density (C5, bottom) packings.

discussion of the v-like ordering). The most efficient way for the next layer to pack is aligned parallel or perpendicular to particles in the first ring. As a result, a distinct peak (i.e., with little spread and no shoulder) is seen at  $\xi \approx 1.5$  (and another at  $\xi \approx 2.5$  for the highest density packings).

#### 6.4. Orientational ordering—local

Table 2 gives values of  $S_2$  local and  $S_4$  local. For comparison, two different criteria were used for identifying neighbor-

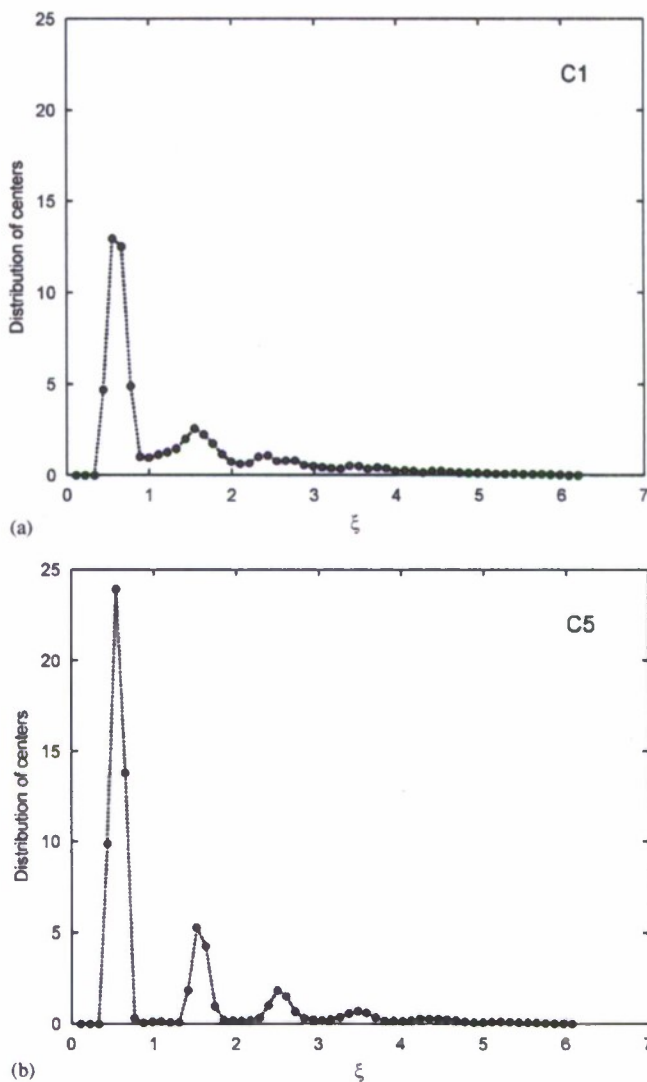


Fig. 7. Wall RDF plots for the minimum- and maximum-density packings.

Table 2

Values of local alignment parameters  $S_2$  and  $S_4$  (two definitions of the local neighborhood for each)

Packing	$S_2$ local (gap $\leq 0.05D_p$ )	$S_2$ local (gap $\leq 0.5D_p$ )	$S_4$ local (gap $\leq 0.05D_p$ )	$S_4$ local (gap $\leq 0.5D_p$ )
C1	−0.025	−0.006	0.193	0.098
C2	0.008	0.000	0.286	0.164
C3	0.013	−0.006	0.302	0.175
C4	−0.012	0.002	0.332	0.231
C5	0.003	−0.013	0.383	0.253

Small values of  $S_2$  indicate negligible nematic ordering. The larger  $S_4$  values indicate local alignment in orthogonal orientations.

ing particles in the ordering computations: gap width  $\leq 0.05D_p$  and gap width  $\leq 0.5D_p$ . The small values of  $S_2$  indicate that local parallel alignment in the bed is *not* the dominant configuration (i.e., end-to-end or side-by-side with parallel axes). The significantly larger values of  $S_4$  show a strong tendency for

Table 3  
Values of global orientational ordering parameters for the five packings

Packing	$I_2$	$I_4$	$S_{2,z}$	$S_{4,z}$	$S_{2,r}$	$S_{4,r}$
C1	0.021	0.054	0.010	−0.049	−0.047	0.064
C2	0.016	0.075	0.001	−0.055	−0.031	0.115
C3	0.027	0.075	0.005	−0.057	−0.002	0.147
C4	0.032	0.151	−0.003	0.130	0.049	0.286
C5	0.026	0.058	0.004	0.032	0.014	0.310

particles to lie parallel and/or orthogonal to one another (side-to-end). This orthogonal configuration is weakest for the C1 packing. As the porosity is lowered (C2–C5), this side-to-end alignment between neighboring particles becomes more prevalent. (It should be emphasized that these results do not indicate the absence of parallel-aligned neighbors, but rather that orthogonal alignment is equally important.)

### 6.5. Orientational ordering—global

Table 3 contains parameters that are used to probe for global orientational ordering in the packing. Both  $I_2$  and  $I_4$  are defined for a Cartesian system and, therefore, provide little insight into global orientational ordering in the cylindrical container. Their values (which are low) are shown here mainly to verify the absence of a gravitational effect that might produce alignment with  $z$  or orthogonal to  $z$ .

The remaining columns in Table 3, when examined together, provide important insight into how the packing structure evolves during densification. The behavior is summarized by four key observations:

- The cylinders tend to align orthogonal to  $r$  (denoted  $r_{\perp}$ ) or parallel to  $r$  (denoted  $r_{\parallel}$ ), where  $r$  is the radial coordinate as defined by the container geometry. This conclusion is based on the finite values of  $S_{4,r}$ .
- The  $r_{\perp}r_{\parallel}$  alignment pattern becomes more pronounced as porosity decreases, as indicated by the increasing values of  $S_{4,r}$  in column 7 of Table 3.
- Alignment in the  $r_{\parallel}$  direction is *not* dominant (relative to  $r_{\perp}$ ), as shown by small  $S_{2,r}$  values.
- Photographs indicate that cylinders in the  $r_{\perp}$  configuration tend to align end to side (orthogonal to one another), suggesting that the  $r_{\perp}r_{\parallel}$  structure corresponds to a three-dimensional orthogonal coordinate system. However, the small magnitudes of  $S_{4,z}$  show that the additional directions are not  $z$  and  $\theta$ .

The fact that the particles exhibit global alignment (i.e., coincident with the global coordinate  $r$ ) suggests that the  $r_{\perp}r_{\parallel}$  alignment originates at the wall. Fig. 8 is a plot of cumulative  $S_{4,r}$  values versus  $\xi_{\text{annulus}}$  (i.e.,  $S_{4,r}$ -cumulative is the average value for all particles in the region  $0 < \xi < \xi_{\text{annulus}}$ ). Not surprisingly, the cumulative  $S_{4,r}$  values are highest when the averaging region is nearest the wall, and the highest values are for the C5 packing.

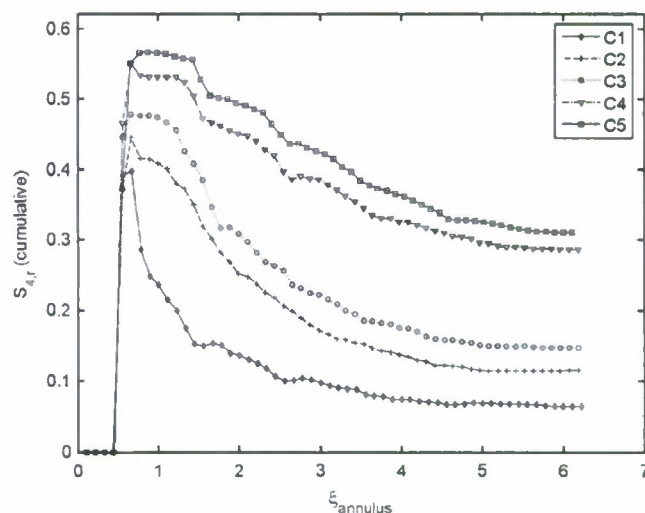


Fig. 8. Plot of bulk  $S_{4,r}$  values for increasingly large averaging volumes adjacent to the wall.

Fig. 9 contains plots of local  $S_{4,r}$  values for the C1 and C5 packings. The same trends are evident: stronger orthogonal ordering exists near the wall. An interesting observation is the negative values of  $S_{4,r}$  at  $\xi = 1$  (and  $\xi = 2, 3$ , and 4 for the C5 packing). The reason is that the integer values of  $\xi$  represent the gaps between rings; the relatively few number of particles that do get stuck in these gaps end up in an anti- $r_{\perp}r_{\parallel}$  configuration in response to their immediate neighborhood (an observation that has been confirmed by visualization of these particles).

Finally, we return to the subject of the fourth bullet above, which suggests that the near-wall particle alignments form an orthogonal coordinate system with an axis aligned with the global coordinate  $r$  but not with  $z$  or  $\theta$ . Visual inspection (see Fig. 1) suggests a v-like structure with particles oriented orthogonal to  $r$  and at roughly  $45^\circ$  with the horizontal plane. Further insight into this matter is obtained using  $S_{4,\alpha}$ . Specifically, we choose a vector on the  $\theta$ - $z$  surface (i.e., an  $r_{\perp}$  vector), and define  $\alpha$  as the angle of this vector with the horizontal. Fig. 10 contains plots of  $S_{4,\alpha}$  versus  $\alpha$  for the C1 and C5 packings. Both plots have maxima at  $\alpha = 45^\circ$ , indicating a preference for particles to align at  $45^\circ$  with the horizontal.

The formation of this v-like structure is repeatable, which suggests a physical origin. We believe it is associated with the dominant ring structures observed in Figs. 6 and 7. Consider a scenario in which the two primary directions for the  $r_{\perp}$  particles are horizontal and vertical (i.e.,  $\theta$  and  $z$  alignment). In this case, the centers of the vertical particles are located at  $\xi = \frac{1}{2}$ . Whereas, the centers of the horizontal particles (and the  $r_{\parallel}$  particles) are located at a distance  $\xi > \frac{1}{2}$  (the exact amount depends on the curvature of the container wall). This arrangement would create a ring in which particles are staggered at two different radial positions as shown by the schematic in Fig. 11. (Consequently, this arrangement would show two peaks in the wall RDF near  $\xi = \frac{1}{2}$ , although it is doubtful that these could be resolved separately using the current experimental technique.)

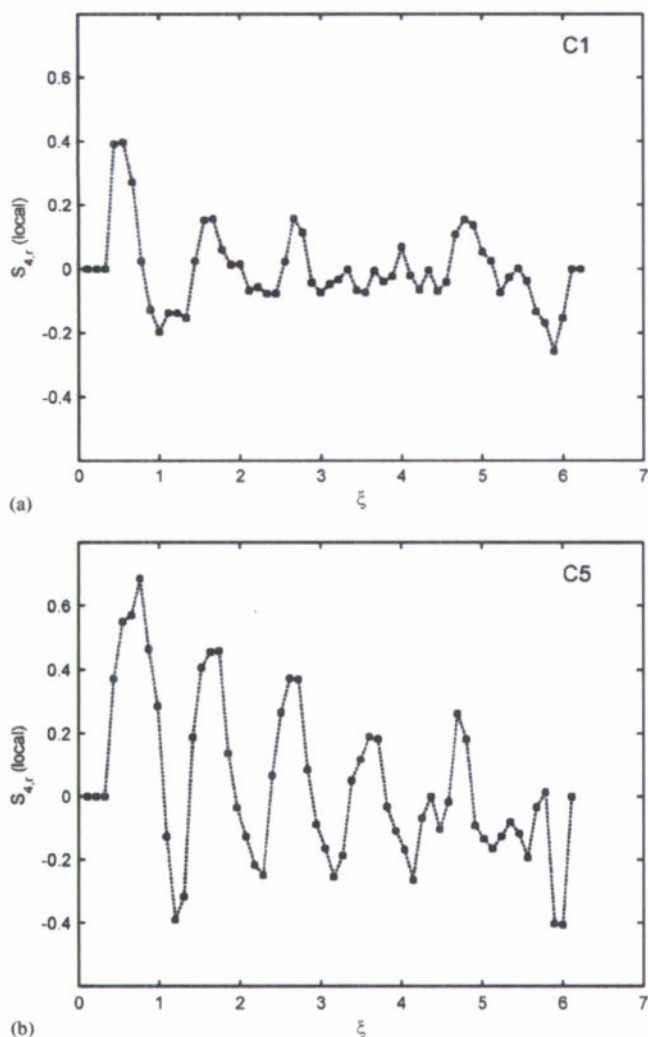


Fig. 9. Local  $S_{4,r}$  versus  $\zeta$  for the minimum- and maximum-density packings. Values that are less than zero indicate an anti- $r_{\perp}r_{\parallel}$  configuration.

This staggered arrangement would constrain the near-wall packing structure because a second ring ( $\zeta \approx 1.5$ ) would be required to interlock with the staggered particles in the first ring, which is impossible because there are fewer particles forming the second ring.

While a  $\alpha_{\max} = 45^\circ$  structure also has a dual RDF peak from the first ring (the  $r_{\parallel}$  particles are located at a larger value of  $\zeta$ ), the radial staggering of particles is minimized. Hence, we hypothesize that the v-like structure forms because it most easily accommodates the dominant ring-like structures observed for these packings.

## 7. Conclusions

X-ray microtomography was successfully used to extract particle-scale structure in a series of fixed beds of equilateral cylinders of diameter 1.8 mm. The resulting data (location and orientation of individual cylinder in the packings) allows a com-

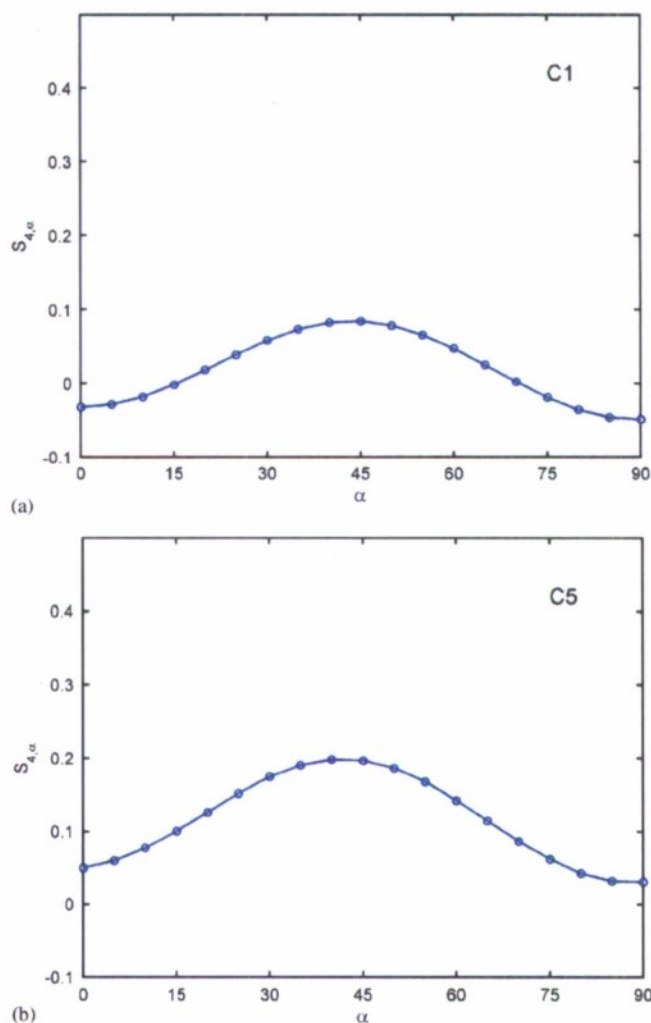


Fig. 10.  $S_{4,x}$  versus  $\alpha$  for the minimum- and maximum-density packings.

prehensive analysis to be made of the evolution of packing structure with increasing packing density.

For the moderate container-diameter to particle-diameter ratio used in these experiments, the packing structures are strongly influenced by the container walls, especially at the highest packing densities. The bulk (interior) porosity has a somewhat larger range than is typically observed with sphere packings. The porosity range near the wall is significantly broader than with spheres. Radial variations in bulk porosity become small as the overall packing density increases.

The most obvious trend in packing structure is the formation of orthogonal alignments between cylinders as the packing density increases. This structure originates at the wall. Hence, the structure evolves to an  $r_{\perp}r_{\parallel}$  configuration, especially near the wall, which indicates that most particles are aligned with the radial coordinate or orthogonal to the radial coordinate. This orthogonal packing structure may reduce the effectiveness of cylindrical catalyst particles with channels through the axial direction, as it could prevent flow into these channels.

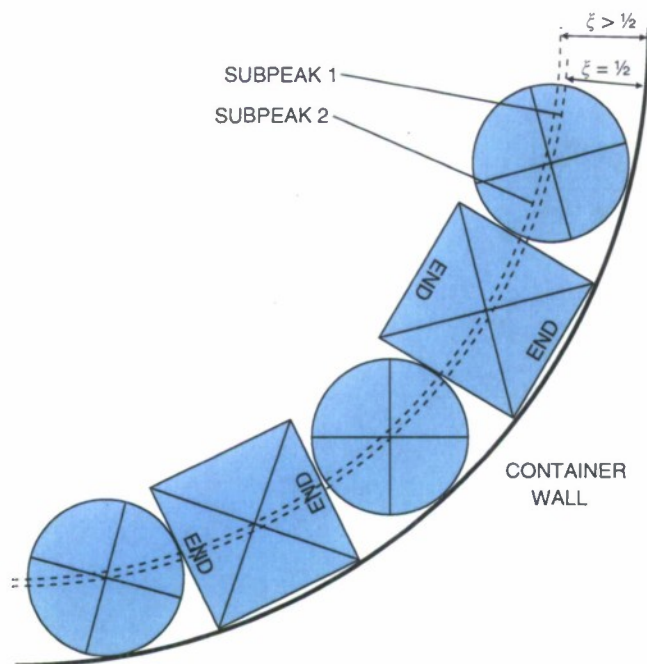


Fig. 11. Schematic showing staggered locations of particle centers caused by different particle alignments against the wall.

## Acknowledgements

This material is based on work funded by the National Science Foundation under Grant Number 0140175. We acknowledge ONR Coastal Geosciences and the Naval Research Laboratory for support that made this work possible. L. Beenken was funded under NSF REU grant EEC-0139656. We acknowledge Clint Willson and Pradeep Bhattad for help with image thresholding.

## References

- Aste, T., Saadatfar, M., Sakellariou, A., Senden, T.J., 2004. Investigating the geometrical structure of disordered sphere packings. *Physica A* 339, 16–23.
- Benyahia, F., 1996. On the global and local structural properties of packed beds of nonequilateral cylindrical particles. *Particulate Science and Technology* 14 (3), 221–237.
- Blaak, R., Frenkel, D., Mulder, B.M., 1999. Do cylinders exhibit a cubic phase? *Journal of Chemical Physics* 110 (23), 11652–11659.
- Clarke, A.S., Jonsson, H., 1993. Structural changes accompanying densification of random hard-sphere packings. *Physical Review E* 47 (6), 3975–3984.
- Coelho, D., Thovet, J.-F., Adler, P.M., 1997. Geometrical and transport properties of random packings of spheres and aspherical particles. *Physical Review E* 55 (2), 1959–1978.
- Dixon, A.G., 1988. Correlations for wall and particle shape effects on fixed bed bulk voidage. *Canadian Journal of Chemical Engineering* 66, 705–708.
- Donev, A., Cisse, I., Sachs, D., Variano, E., Stillinger, F.H., Connelly, R., Torquato, S., Chaikin, P.M., 2004. Improving the density of jammed disordered packings using ellipsoids. *Science* 303, 990–993.
- Evans, K.E., Gibson, A.G., 1986. Prediction of the maximum packing fraction achievable in randomly oriented short-fibre composites. *Composite Science and Technology* 25, 149–162.
- Foumeny, E.A., Roshani, S., 1991. Mean voidage of packed beds of cylindrical particles. *Chemical Engineering Science* 46 (9), 2363–2364.
- Kondelik, P., Horak, J., Tesarova, J., 1968. Heat and mass transfer in heterogeneous catalysis: variation of local void fraction in randomly packed beds of equilateral cylinders. *Industrial & Engineering Chemistry Process Design and Development* 7, 250–252.
- Kubie, J., 1988. Influence of containing walls on the distribution of voidage in packed beds of uniform spheres. *Chemical Engineering Science* 43 (6), 1403–1405.
- Lindquist, W.B., Lee, S., 1996. Medial axis analysis of void structure in three-dimensional tomographic images of porous media. *Journal of Geophysical Research* 101, 8297–8310.
- Liu, G., Thompson, K.E., 2000. Influence of computational domain boundaries on internal structure in low-porosity sphere packings. *Powder Technology* 113, 185–196.
- Lumay, G., Vandelwalle, N., 2004. Compaction of anisotropic granular materials: experiments and simulations. *Physical Review E* 70, 051314(1–5).
- Marchot, P., Toye, D., Crine, M., Pelsser, A.-M., L'Homme, G., 1999. Investigation of liquid maldistribution in packed columns by X-ray tomography. *Transactions of the Institution of Chemical Engineers* 77 (A), 511–518.
- Milewski, J.V., 1973. A study of the packing of milled fiberglass and glass beads. Presented at the Reinforced Plastics/Composite Institute 28th Annual Conference and Exhibition.
- Montillet, A., Le Coq, L., 2001. Characteristics of fixed beds packed with anisotropic particles—Use of image analysis. *Powder Technology* 121, 138–148.
- Mueller, G.E., 2005. Numerically packing spheres in cylinders. *Powder Technology* 159 (2), 105–110.
- Nardin, M., Papirer, E., Schultz, J., 1985. Contribution a l'Etude des Empilements au Hasard de Fibres et/ou de Particules Spheriques. *Powder Technology* 44, 131–140.
- Nijemeisland, M., Dixon, A.G., Stitt, E.H., 2004. Catalyst design by CFD for heat transfer and reaction in steam reforming. *Chemical Engineering Science* 59 (22–23), 5185–5191.
- Philippe, A.P., 1996. The random contact equation and its implications for (colloidal) rods in packings, suspensions, and anisotropic powders. *Langmuir* 12, 1127–1133.
- Reyes, S.C., Iglesia, E., 1991. Monte Carlo simulations of structural properties of packed beds. *Chemical Engineering Science* 46 (4), 1089–1099.
- Richard, P., Philippe, P., Fabrice, B., Bourles, S., Thibault, X., Bideau, D., 2003. Analysis by X-ray microtomography of a granular packing undergoing compaction. *Physics Review E* 68, 020301/1–020301/4.
- Roblee, L.H.S., Baird, R.M., Tierney, J.W., 1958. Radial porosity variations in packed beds. *A.I.Ch.E. Journal* 4 (4), 460–464.
- Roshani, S., 1990. Elucidation of local and global structural properties of packed bed configurations. Ph.D. Thesis, University of Leeds, UK.
- Seidler, G.T., Martinez, G., Seeley, L.H., Kim, K.H., Behne, E.A., Zaranek, S., Chapman, B.D., Heald, S.M., Brewster, D.L., 2000. Granule-by-granule reconstruction of a sandpile from X-ray microtomography data. *Physics Review E* 62 (6), 8175–8181.
- Sharma, S., Mantle, M.D., Gladden, L.F., Winterbottom, J.M., 2001. Determination of bed voidage using water substitution and 3D magnetic resonance imaging, bed density and pressure drop in packed bed reactors. *Chemical Engineering Science* 56 (2), 587–595.
- Stephenson, J.L., Stewart, W.E., 1986. Optical measurements of porosity and fluid motion in packed beds. *Chemical Engineering Science* 41 (8), 2161–2170.
- Theuerkauf, J., Witt, P., Schwesig, D., 2006. Analysis of particle porosity distribution in fixed beds using the discrete element method. *Powder Technology* 165, 92–99.
- Thompson, K.E., Willson, C.S., Zhang, W., 2006. Quantitative computer reconstruction of particulate materials from microtomography images. *Powder Technology* 163, 169–182.
- Torquato, S., Truskett, T.M., Debenedetti, P.G., 2000. Is random close packing of spheres well defined? *Physical Review Letters* 84 (10), 2064–2067.
- Villarruel, F.X., et al., 2000. Compaction of rods: relaxation and ordering in vibrated, anisotropic granular material. *Physical Review E* 61 (6), 6914–6921.

- Wang, Z., Afacan, A., Nandakumar, K., Chuang, K.T., 2001. Porosity distribution in random packed columns by gamma ray tomography. *Chemical Engineering and Processing* 40, 209–219.
- Williams, S.R., Philipse, A.P., 2003. Random packings of spheres and spherocylinders simulated by mechanical contraction. *Physical Review E* 67, 051301(1–9).
- Weitz, D.A., 2004. Packing in the spheres. *Science* 303, 968–969.
- Wellington, S.L., Vinegar, H.J., 1987. X-ray computerized tomography. *Journal of Petroleum Technology* 39 (8), 885–898.
- Zhang, W., Thompson, K.E., Reed, A.H. Partial ordering during the densification of packings of cylindrical particles (in review).
- Zou, R.P., Yu, A.B., 1995. The packing of spheres in a cylindrical container: the thickness effect. *Chemical Engineering Science* 50 (9), 1504–1507.